15

Modelling of Heat Transfer and Phase Transformations in the Rapid Manufacturing of Titanium Components

António Crespo
Instituto Superior Técnico
Portugal

1. Introduction

Over the last thirty years a new generation of manufacturing processes have been developed whereby fabrication takes place by the sequential addition of material at specific locations on a layer-by-layer basis to produce near-net-shape three-dimensional parts. These processes are generically known as solid freeform fabrication or rapid manufacturing, and their most prominent features are fast delivery times, material wastage reduction and the ability to produce parts directly from a CAD file in a single fabrication step without the need for hard tooling. These characteristics lead to lower costs and faster production cycles than those of hard-tooling based methods, and have made solid freeform fabrication an attractive choice for the production of customised one-of-a-kind parts, prototyping and short-run production. For the manufacture of metallic components these techniques involve the use of a localised energy source, typically a laser beam, to consolidate layers of metallic materials supplied in the form a pre-placed powder bed, blown powder stream or wire feeding. By scanning the interaction zone of the energy source and the material over a substrate and according to a previously defined trajectory, a track of resolidified material is produced and the overlapping of tracks enables the manufacture of near-net-shape components, as shown schematically in Figure 1.

One important feature of rapid manufacturing techniques is that, as a result of layer overlap during part buildup, the deposited material undergoes consecutive thermal cycles with a duration and amplitude which depend on the processing parameters and on the shape and dimensions of the part being manufactured. These thermal cycles induce phase transformations in the material leading to a progressive modification of its microstructure and properties. Since the thermal history varies from point to point in the part, the material will in general present complex distributions of microstructure and properties. To optimise the manufacturing process to obtain parts fulfilling specific requirements, the influence of the processing conditions and build-up strategy on the final microstructure and properties of the material must be assessed. The complexity of the thermal cycles taking place during the manufacture of components and the impossibility of directly monitoring the thermal and microstructural evolution of the material during the fabrication process make empirical or experimental build-up strategy optimisation impractical. However, the optimisation of the process can be carried out efficiently using a computational approach based on a model

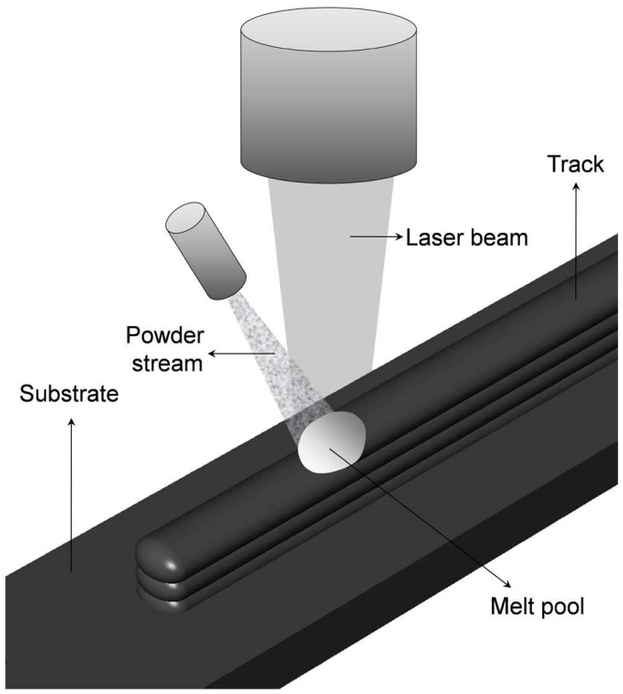

Fig. 1. Rapid manufacturing using a laser beam to consolidate blown powder particles into a final part

that simulates the microstructure formation mechanisms in the material, in particular the phase transformations caused by the heat and mass transfer phenomena that take place during fabrication. Such a model should use as input the processing parameters and the part shape and dimensions to predict the final microstructure and properties distributions in the manufactured part. This type of approach provides a cheap and rapid way of optimising the manufacturing process and obtaining parts fulfilling unique and specific properties requirements. Several researchers such as L. Costa (Costa et al., 2005), S. M. Kelly (Kelly & Kampe, 2004b), Toyserkani et al. (Toyserkani et al., 2004), have successfully used computational approaches to analyse the influence of the processing parameters on several aspects of the process, such as the heat transfer mechanisms, the microstructure formation processes or the evolution of the properties of the material, among others (Crespo et al., 2006; Labudovich et al., 2003; Vasinonta et al., 2001; Wang et al., 2008).

In addition to microstructural transformations, the consecutive thermal cycles imposed on the material are also responsible for the accumulation of internal stresses in parts produced by rapid manufacturing techniques. During the fabrication process, the thermal cycles experienced by the material will give rise to thermal expansion and contraction. Since the deposited material is cyclically subjected to steep temperature variations, the thermal expansion gradients ocurring in the material give rise to the development of internal stresses in the workpiece. These stresses can be high enough to cause yield in some regions or lead to complex residual stresses patterns in the final parts. The study of the development of residual stresses during rapid manufacturing processes has been the subject of several investigations aimed at acquiring a thorough insight into this phenomenon and at establishing processing parameters sets and build-up strategies

conducive to mechanically sound components (Crespo et al., 2008; Deus & Mazumder, 2006; Ghosh & Choi, 2005; Kahlen & Kar, 2001; Labudovich et al., 2003). Although the study of residual stresses formation during manufacture is out of the scope of the present work, the model presented in this chapter has been extended to study these phenomena and a detailed description of the methodology can be found in the work of A. Crespo (Crespo, 2010).
This chapter reports the development of a finite element thermo-kinetic model that couples heat transfer calculations with phase transformation kinetics theory to investigate the influence of the build-up strategy and processing parameters on the distributions of microstructure and properties of titanium parts manufactured by rapid manufacturing processes. The model was validated by comparing its predictions for the phase constitution, Young's modulus and hardness distributions with experimental results measured on parts fabricated by a laser based rapid manufacturing technique, and used to construct processing maps relating the deposition parameters to the microstructure and properties of the parts.

2. Modelling of heat transfer in rapid manufacturing processes

Rapid manufacturing processes are characterised by the continuous addition of material on a layer-by-layer basis to produce a final component. In order to process the different layers into a consolidated part an energy source is typically used to heat up and melt the feedstock material before incorporation into the part (Figure 1). This type of manufacturing subjects the processed material to consecutive thermal cycles which induce a sequence of phase transformations that alter the microstructure and properties of the material, and which, if not properly controlled, may render the final parts useless. Therefore a critical aspect of additive manufacturing is the control of the different heat transfer phenomena that take place during build-up and which determine the properties and quality of the final parts.

2.1 Heat transfer equations

The phase transformations during rapid manufacturing are determined by the thermal history of the material, which is the result of energy absorption by the material, heat conduction within the workpiece being built and heat losses by convection and radiation to the environment. The temperature field evolution within the material can be calculated by solving the three-dimensional heat conduction equation. Thermal conduction in an isotropic solid region Ω is a time dependent 3-D problem described by the following partial differential equation:

$$\rho C_p \frac{dT(\vec{r},t)}{dt} = \nabla \left[k \nabla T(\vec{r},t)\right] + Q, \tag{1}$$

where $T(\vec{r},t)$ is the temperature $(^\circ C)$, ρ the density of the solid (kgm^{-3}), k the thermal conductivity $(W^\circ C^{-1}m^{-1})$, C_p the specific heat $(J^\circ C^{-1}Kg^{-1})$ and Q a generic internal heat generation rate (Wm^{-3}) which can account, for example, for phenomena associated with latent heats of transformation. The thermal properties of materials are usually temperature dependant, that is: $\rho = \rho(T)$, $k = k(T)$ and $C_p = C_p(T)$. To apply the heat conduction equation to time-dependants problems, such as simulating a fabrication process, an initial condition specifying the initial temperature distribution in the part must also be provided:

$$T(\vec{r}, t=0) = T_0(\vec{r}), \quad \vec{r} \in \Omega. \tag{2}$$

Additionally, the influence of the energy source used to process the material has to be taken into consideration. The best way to model the interaction between the heat source and the material depends on the particular characteristics of the energy source being used such as its power, power density, shape and the way it is absorbed or transferred into the material. Probably the most common way of processing metallic materials for rapid manufacturing purposes is to utilise a laser beam. Assuming, for example, a gaussian distribution of the laser beam power , the energy input into the material can be described by:

$$q_{laser} = \alpha \frac{2.P}{\pi.r_l^2} exp[-\frac{2.r^2}{r_l^2}], \tag{3}$$

where P is the laser beam power, α the absorptivity of the material to the radiation being used, r_l the spot radius of the laser beam and r the distance to its centre, respectively. Energy losses to the environment by convection and radiation are described by:

$$Q_{convection} = h\left[T(\vec{r},t) - T_\infty\right] \tag{4}$$

$$Q_{radiation} = \epsilon\sigma_s\left[T^4(\vec{r},t) - T_\infty^4\right], \tag{5}$$

where h, ϵ, σ_s and T_∞ are the convective heat transfer coefficient, emissivity, Stefan-Boltzmann constant and temperature of the surrounding environment (room temperature), respectively. On the surface of the workpiece, the balance between the heat lost to the environment by convection and radiation and the energy absorbed from the laser radiation can be written as:

$$-k\nabla T\vec{n} = h\left[T(\vec{r},t) - T_\infty\right] + \epsilon\sigma_s\left[T^4(\vec{r},t) - T_\infty^4\right] - q_{laser}, \quad \vec{r} \in \Gamma, \tag{6}$$

where Γ represents the surface (or boundary) of the solid region Ω and $\vec{n}$ is the unitary vector normal to the surface Γ.

2.2 The finite element method

Although the mathematical description of heat transfer during rapid manufacturing processes is easy to formulate, its solution can rarely be analytically determined. In particular, rapid manufacturing processes involve the continuous incorporation of material into the parts being built, which means that the shape of the part is continuously changing and an adequate mathematical description of this type of process must also account for an evolving geometry. The finite element method has been successfully used by previous authors (Costa et al., 2005; Deus & Mazumder, 2006; Kelly & Kampe, 2004b; Toyserkani et al., 2004) to study additive manufacturing processes. The finite element method is a numerical technique for calculating approximate solutions to algebraic, differential and integral equations for which analytical solutions cannot be found. It is frequently applied to physical and engineering problems in areas such as structural mechanics, dynamics, fluid mechanics and heat transfer. This method can efficiently handle complicated geometries and account for non-uniform properties and boundary conditions, and is easily implemented in computer programs to solve complex simulation problems, taking advantage of the large computational power presently available, therefore making this technique a prime choice to study heat transfer during rapid manufacturing processes.

Calculating the solution to a problem using the finite element method is accomplished by using several mathematical tools and can be summarised by the following sequence of steps (Desai & Abel, 1972; Reddy, 2006; Zienkiewicz & Taylor, 2000):

1. the physical domain of the problem being solved is partitioned into a collection of simple geometrical sub-domains called finite elements;
2. in each element, the solution is approximated by a linear combination of adequately chosen interpolation functions and time dependant temperature values at the nodes of the elements: $T(\vec{r},t) \approx \sum_{j=1}^{n} T_j(t)\psi_j(\vec{r})$, with the governing equations of the problem being used to establish algebraic relations between the unknown nodal temperatures $T_j(t)$;
3. the algebraic equations developed for the different elements are assembled by requiring the continuity of $T(\vec{r},t)$ and the balance of certain relevant physical quantities at the interface between neighbouring elements. This produces a system of equations which can be solved to find the coefficients $T_j(t)$ and produce an approximate solution to the problem.

The approximate solution differs from the exact solution due to the approximations made in each of the three steps described above: in the first step errors are introduced because a continuous physical domain is represented by a finite element mesh that does not match it exactly; in the second step errors arise from approximating the exact solution over each element by a finite sum of functions; the solution of the system of assembled equations in the third step usually requires numerical integration, which is another source of error. The overall error in the computed solution can be minimised, for example, by refining the mesh to ensure a more accurate representation of the physical domain (first step), by using a better approximation to the local solution during the development of the algebraic equations in each element (second step) and by defining stricter convergence criteria in the numerical integration (third step). However, error reduction is achieved at the expense of computation time and usually a compromise has to be accepted between the accuracy of the solution and the time to compute it .

In the finite element method the equations governing heat transfer in the elements are expressed in terms of a variational formulation, typically the weak form of the heat conduction equation. Although the weak form of the heat conduction equation will not be derived here, it produces the following set of equations for each element (Reddy, 2006):

$$\sum_{j=1}^{n}\left(M_{ij}^{e}\frac{dT_j^e(\vec{r},t)}{dt}+K_{ij}^{e}T_e^e(\vec{r},t)\right)-Q_i^e-q_i^e=0, \qquad i=1,...,n, \tag{7}$$

where the superscript e is an identification label for each element in the mesh and n is the order of the interpolation functions used to approximate the solution. M_{ij}^e, K_{ij}^e, Q_i^e and q_i^e are defined by:

$$\begin{aligned} M_{ij}^{e} &= \int_{\Omega^e}\rho C\psi_i\psi_j dV, \quad K_{ij}^{e}=\int_{\Omega^e}k\nabla\psi_i.\nabla\psi_j dV \\ Q_i^{e} &= \int_{\Omega^e}\psi_i Q(\vec{r},t)dV, \quad q_i^{e}=\int_{\Gamma}\psi_i\left[q_{laser}-h\left(T-T_\infty\right)-\epsilon\sigma_s\left(T^4-T_\infty^4\right)\right]dS, \end{aligned} \tag{8}$$

where the dependencies of T on $\vec{r}$ and t have been omitted for simplicity. $Q(\vec{r},t)$ represents the heat flux across the common surfaces of neighbouring elements and the equations of the

different elements are assembled together by requiring the balance of this flux from each element to its neighbours and the continuity of the temperature field $T(\vec{r},t)$. This system of equations is commonly written in matrix form as:

$$\mathbf{M}^e\dot{\mathbf{T}}^e + \hat{\mathbf{K}}^e\mathbf{T} = \mathbf{F}^e, \tag{9}$$

where

$$\begin{aligned}
\mathbf{M}^e &= M_{ij}^e \\
\hat{\mathbf{K}}^e &= K_{ij}^e - I_{ij}\int_{\Gamma_2}\psi_i\left(-h - \epsilon\sigma_s T^3\right)dS \\
\mathbf{F}^e &= Q_i^e + \int_{\Gamma_2}\psi_i\left(q_{laser} + hT_\infty + \epsilon\sigma_s T_\infty^4\right)dS,
\end{aligned} \tag{10}$$

with I_{ij} the identity matrix.
The equations of the single elements are assembled by summing the element equations corresponding to the same nodes:

$$\mathbf{M} = \sum_e \mathbf{M}^e, \quad \hat{\mathbf{K}} = \sum_e \hat{\mathbf{K}}^e, \quad \mathbf{F} = \sum_e \mathbf{F}^e, \tag{11}$$

resulting in the global equation:

$$\mathbf{M}\dot{\mathbf{T}} + \hat{\mathbf{K}}\mathbf{T} = \mathbf{F}. \tag{12}$$

The system of ordinary differential equations expressed by the matrix equation 12 must be completed by providing an initial condition $\mathbf{T}(0) = \mathbf{T}_0$. Therefore we seek to solve the initial value problem defined by:

$$\begin{aligned}
&\mathbf{M}\dot{\mathbf{T}} + \hat{\mathbf{K}}\mathbf{T} = \mathbf{F}, \\
&\mathbf{T}(0) = \mathbf{T}_0.
\end{aligned} \tag{13}$$

This can be converted to a system of algebraic equations by dividing the time domain into steps and using finite differences to approximate the time derivatives. Equation 13 can be solved by considering a weighted average of the time derivatives at two consecutive time steps (t_s and t_{s+1}) and developing an iterative procedure to find the solution at each step (Reddy & Gartling, 1994):

$$\begin{aligned}
\mathbf{T}(t_{s+1}) &= \mathbf{T}(t_s) + \dot{\mathbf{T}}(t_{s+\alpha})(t_{s+1} - t_s), \\
\dot{\mathbf{T}}(t_{s+\alpha}) &= (1-\alpha)\dot{\mathbf{T}}(t_s) + \alpha\dot{\mathbf{T}}(t_{s+1}).
\end{aligned} \tag{14}$$

Different choices of α lead to well known approximation schemes that are commonly found in the literature:

$\alpha = 0$,	forward difference, or Euler, scheme
$\alpha = 1/2$,	Crank-Nicholson scheme
$\alpha = 2/3$,	Galerkin scheme
$\alpha = 1$,	backward difference scheme.

Substitution of Equation 13 in Equation 14 yields the solution to the problem:

$$\begin{aligned}\mathbf{T}(t_{s+1}) = \mathbf{T}(t_s) + (1-\alpha)\mathbf{M}^{-1}\left[\mathbf{T}(t_s)\right]\left\{\mathbf{F}\left[\mathbf{T}(t_s)\right] - \hat{\mathbf{K}}\left[\mathbf{T}(t_s)\right]\mathbf{T}(t_s)\right\}(t_{s-1}-t_s) \\ \alpha\mathbf{M}^{-1}\left[\mathbf{T}(t_{s+1})\right]\left\{\mathbf{F}\left[\mathbf{T}(t_{s+1})\right] - \hat{\mathbf{K}}\left[\mathbf{T}(t_{s+1})\right]\mathbf{T}(t_{s+1})\right\}(t_{s-1}-t_s).\end{aligned} \tag{15}$$

In general Equation 15 leads to an implicit scheme that requires iterative solutions to be found within each time step. The forward difference method is the only one of the above which is an explicit method and is the easiest to implement. It results in a simple iterative solution where $\mathbf{T}(t_{s+1})$ is readily obtained from the solution at the previous step $\mathbf{T}(t_s)$, and is given by:

$$\mathbf{T}(t_{s+1}) = \mathbf{T}(t_s) + \mathbf{M}^{-1}\left[\mathbf{T}(t_s)\right]\left\{\mathbf{F}\left[\mathbf{T}(t_s)\right] - \hat{\mathbf{K}}\left[\mathbf{T}(t_s)\right]\mathbf{T}(t_s)\right\}(t_{s-1}-t_s). \tag{16}$$

Starting from $\mathbf{T}(0) = \mathbf{T}_0$, the solution at subsequent steps can be calculated from Equation 16. Equation 16 is a general expression that relates the temperatures at various points of a geometry by requiring the balance of heat fluxes across the boundaries between neighbouring elements and the continuity of the temperature field, governed by the weak form of the heat conduction equation. The temperature evolution during additive manufacture for a component of arbitrary geometry can be found by implementing Equation 16 as a computer code.

2.3 Representation of the physical domain

A finite element model should ideally describe the geometry of the substrate and the tracks as closely as possible. Frequently the substrate is a parallelepiped which can be easily represented in the form of a finite element mesh. However, it is more difficult to develop a mesh which allows a step wise description of the deposition of tracks with complex 3-D features, such as curved cross sections or curved fronts. To describe the full detail of track overlap during manufacture, the finite element mesh becomes complex and requires many elements for the proper representation of the 3-D features of the tracks, as shown in Figure 2.a.

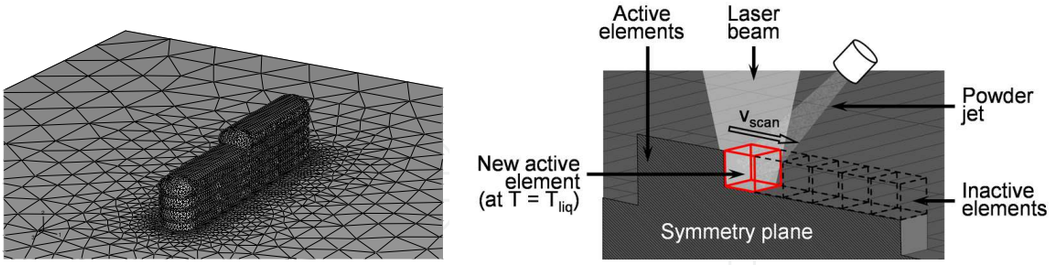

Fig. 2. (a) Finite element mesh of substrate and tracks. (b) Step-wise approach to simulate the addition of material. New elements are activated at liquidus temperature. Adapted from Crespo and Vilar (Crespo & Vilar, 2010)

One commonly applied strategy to reduce the number of elements is to use a fine mesh only in regions which have complex geometries or where thermal gradients are expected to be high (in the vicinity of interaction zone between the energy source and the material), while using a coarser mesh away from these zones (Figure 2.a). The level of refinement shown in Figure

2.a is necessary if certain aspects of the fabrication process such as the formation of hot-spots or the solidification rate must be predicted, which require the precise shape of the melt pool and of the incorporated material to be taken into account (Bontha et al., 2006; Crespo et al., 2006). When the purpose of the simulation does not demand such a rigorous description of the track shape, simpler meshes may be used by assuming that the shapes of the melt pool and of the tracks can be approximated by simpler geometries. This has the advantage of reducing considerably the number of elements in the mesh, and as a consequence the number of calculations and the computational time necessary to resolve the problem. Several authors have developed finite element models which use simple cubic elements to simulate the addition of material and have demonstrated the validity of this approach (Costa et al., 2005; Deus & Mazumder, 2006), which is also used in the present work. If the deposition if assumed to take place in the mid-plane of the substrate, there is a symmetry plane in respect of which heat flow is symmetrical and one needs only consider half the geometry of the problem, as illustrated in Figure 2.b, further reducing the computational time needed to achieve the solution for the heat transfer problem.

In the model proposed in this chapter, Equation 16 is solved iteratively for each element in the step by step approach described in the previous section. Addition of material is taken into account by activating at each new time step elements with a volume corresponding to the volume of material incorporated into the part during the duration of that step (Figure 2.b), based on a methodology first presented by Costa et al. (Costa et al., 2005). Taking into consideration the results of Neto and Vilar (Neto & Vilar, 2002), who showed that in blown powder laser cladding the powder flying through the laser beam often reaches the liquidus temperature before impinging into the part, the newly active elements are assumed to be at the liquidus temperature.

3. Phase transformations during the rapid manufacturing of titanium components

Titanium alloys are being increasingly used in a wide range of applications due to properties such as high strength to weight ratio, excellent corrosion resistance, high temperature strength and biocompatibility. These properties have made titanium alloys a widespread material in industries such as the aerospace, automotive, biomedical, energy production, chemical, off-shore and marine industries, among others (Boyer et al., 1994; Donachie, 2004).

In the last decade, the Ti-6Al-4V alloy has accounted for more than half the production of titanium alloys worldwide, a market estimated at more than $2,000 million (Leyens & Peters, 2003). This predominance is mainly due to Ti-6Al-4V having the best all-around mechanical characteristics for numerous applications. This alloy is extensively used in the aerospace industry for the production of turbine engines and airframe components, which account for approximately 80% of its total usage. Additionally, Ti-6Al-4V presents excellent biocompatibility and osseointegration properties which have made it a natural choice as a biomaterial for the fabrication of implants and other biomedical devices (Brunette, 2001; Yoshiki, 2007). When compared to other materials usually used for the same purpose, such as stainless steel or CoCr alloys, Ti-6Al-4V allows the production of much stronger, lighter and less stiff implants and with improved biomechanical behaviour.

Ti-6Al-4V is an α/β titanium alloy that contains 6% of the α-phase stabilising element Al, and 4% of the β-phase stabilising element V in its composition. As a result of the combined effect of these two alloying elements, the equilibrium microstructure of Ti-6Al-4V consists of

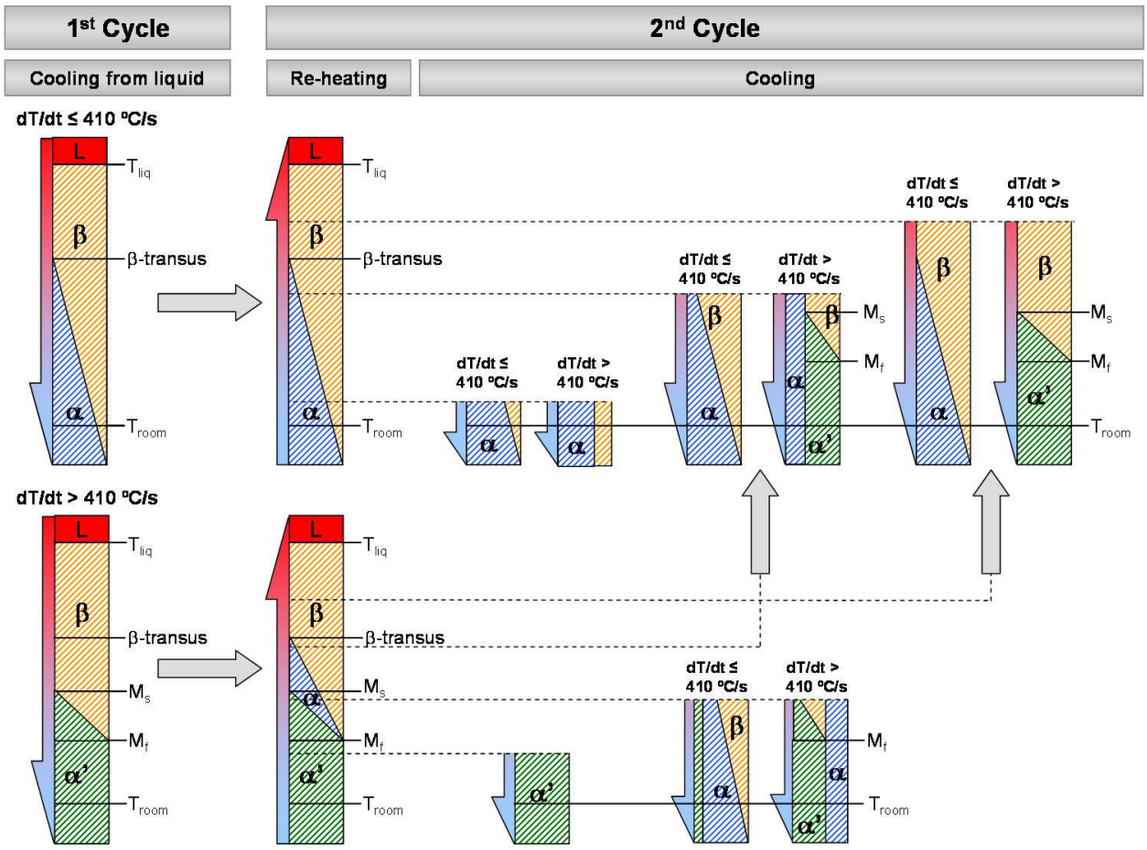

Fig. 3. Phase transformations during rapid manufacturing of Ti-6Al-4V.

a mixture of α and β phases for temperatures between room temperature and 980 °C, which is called the β-transus temperature (Polmear, 1989). The proportion of β phase in equilibrium depends on the temperature, varying from approximately 0.08 at room temperature to 1.00 at the β-transus, and is given by (R. Castro, 1966):

$$\begin{aligned} f_{\alpha}^{eq}(T) &= \begin{cases} 0.925 - 0.925.e^{[0.0085(980-T)]}, & T \leq 980^{\circ}C/s \\ 0, & T > 980^{\circ}C/s \end{cases} \\ f_{\beta}^{eq}(T) &= 1 - f_{\alpha}^{eq}(T), \end{aligned} \tag{17}$$

with T in °C. In titanium alloys the β-transus temperature represents the minimum temperature above which β is the only equilibrium phase. The phase transformations that can occur due to the consecutive thermal cycles generated by layer overlap during build-up of parts by rapid manufacturing are represented in the diagram of Figure 3.

3.1 Phase transformations during cooling from the liquid phase

Prior to incorporation into the part the feedstock Ti-6Al-4V is melted, and after solidification its structure consists of β phase. During cooling to room temperature β may undergo two different phase transformations depending on the cooling rate.

3.1.1 Diffusional transformations

For cooling rates lower than 410 °C/s, a $\beta \rightarrow \alpha$ transformation takes place controlled by a diffusional mechanism, starting at the β-transus temperature (980 °C). At room temperature, the final microstructure consists of α and β because the transformation does not reach completion. In isothermal condition the kinetics of this transformation is described by the Johnson-Mehl-Avrami (JMA) equation:

$$f(t) = 1 - exp\left(-jt^n\right), \tag{18}$$

where $f_\alpha(t)$, k and n are the fraction of α formed after time t, the reaction rate constant and the Avrami exponent, respectively. The values for k and n were determined as a function of the temperature by Malinov et al. (Malinov, Markovsky, Sha & Guo, 2001). The Johnson-Mehl-Avrami equation cannot be used to describe the kinetics of anisothermal transformations because the reaction rate constant k depends on the temperature. As a consequence, the direct integration of the Johnson-Mehl-Avrami equation to calculate the transformed proportion during cooling is not possible. Nevertheless, good results have been achieved by generalising the Johnson-Mehl-Avrami equation to anisothermal conditions using the additivity rule (Malinov, Guo, Sha & Wilson, 2001; S. Denis, 1992). In this method, continuous cooling is replaced by a series of small consecutive isothermal steps where the Johnson-Mehl-Avrami equation can be applied. During the first isothermal time step, $[t_0, t_1[$, at temperature T_0, the fraction of α phase formed can be calculated from Equation 18 and is given by:

$$f_\alpha(t_1) = \left\{1 - exp\left[-k_0(t_1 - t_0)^{n_0}\right]\right\}.f_\alpha^{eq}(T_0) \tag{19}$$

where k_0 and n_0 are the reaction rate constant and Avrami exponent at the temperature T_0, respectively. In the next interval, $[t_1, t_2[$, the transformation is assumed to take place at the temperature T_1, but one must take into consideration the fact that a fraction $f_\alpha(t_1)$ of α phase has already formed in the previous step. Substituting the fraction $f_\alpha(t_1)$ in Equation 18, one can calculate the time it would take to form the proportion $f_\alpha(t_1)$ of α phase if the whole transformation had taken place at the temperature T_1:

$$t_1^f = \sqrt[n_1]{-\frac{ln[1 - f_\alpha(t_1)/f_\alpha^{eq}(T_1)]}{k_1}}, \tag{20}$$

where k_1 and n_1 are the reaction rate constant and Avrami exponent at the temperature T_1. The additivity principle requires that t_1^f be the initial time for the new transformation step. Therefore, for the time interval $[t_1, t_2[$, one gets:

$$f_\alpha(t_2) = \left\{1 - exp\left[-k_1(t_1^f + t_2 - t_1)^{n_1}\right]\right\}.f_\alpha^{eq}(T_1). \tag{21}$$

Equation 21 can be generalised for an arbitrary time step $[t_s, t_{s+1}[$ at temperature T_s, leading to a fraction of α formed during that step given by:

$$f_\alpha(t_{s+1}) = \left\{1 - exp\left[-k_s(t_s^f + t_{s+1} - t_s)^{n_s}\right]\right\}.f_\alpha^{eq}(T_s), \tag{22}$$

where t_s^f is given by:

$$t_s^f = \sqrt[n_s]{-\frac{ln[1 - f_\alpha(t_s)/f_\alpha^{eq}(T_s)]}{k_s}}. \tag{23}$$

The application of the additivity rule to the Johnson-Mehl-Avrami equation is illustrated in Figure 4.

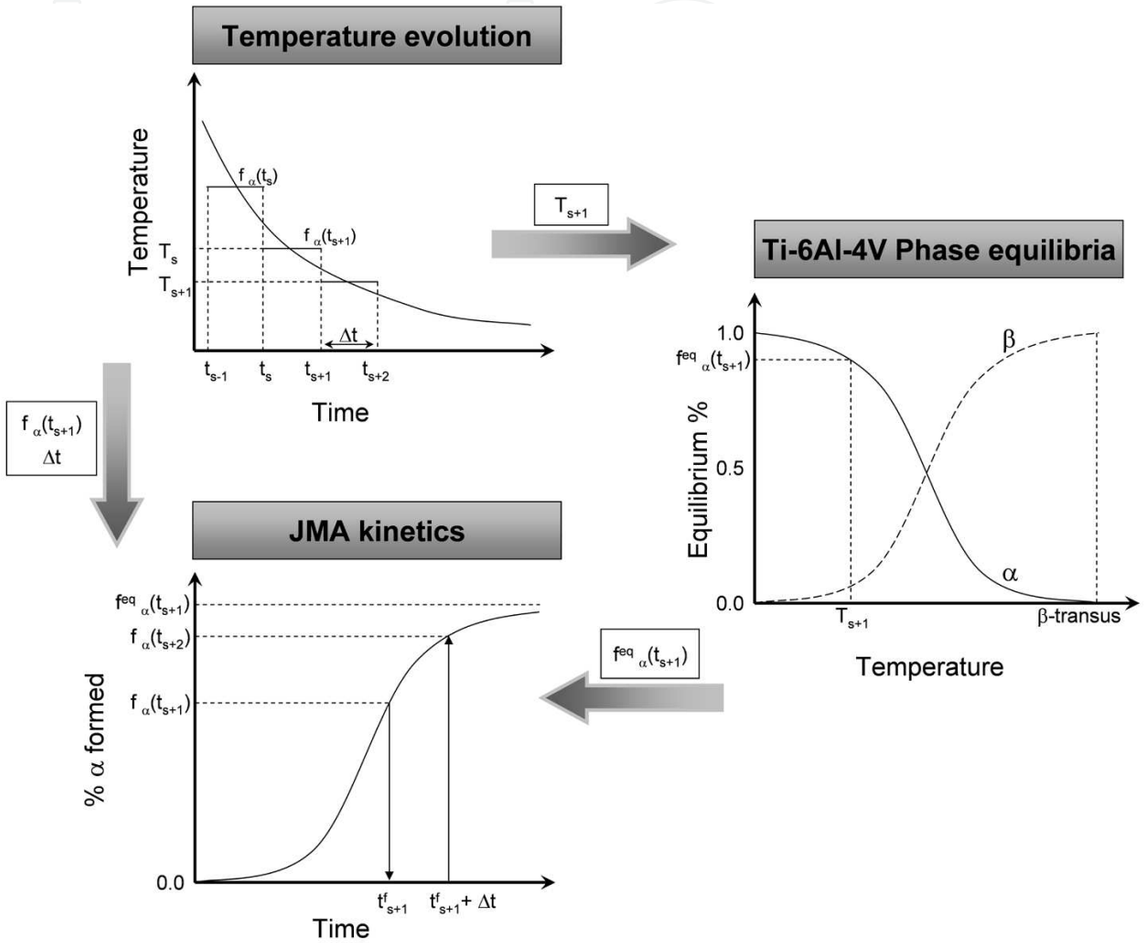

Fig. 4. Generalization of the Johnson-Mehl-Avrami equation for anisothermal transformations.

3.1.2 Martensitic transformations

For cooling rates higher than 410 °C/s the $\beta \rightarrow \alpha$ diffusional transformation is suppressed and β decomposes by a martensitic transformation. The proportion of β transformed into martensite (α') depends essentially on the undercooling below the martensite start temperature (M_s) and is given by (Koistinen & Marburger, 1959):

$$f_{\alpha'}(T) = 1 - exp\left[-\gamma(M_s - T)\right]. \tag{24}$$

The values of γ, M_s and M_f used in the present work (0.015 °C^{-1}, 650 °C and 400 °C respectively) were calculated on the basis of the results of Elmer et al. (Elmer et al., 2004). If the material cools below M_f its microstructure is fully martensitic.

3.2 Phase transformations during re-heating

When new layers are added to the part, the previously deposited material undergoes heating/cooling cycles that may induce microstructural and properties changes. If the microstructure formed in first thermal cycle is composed of $\alpha + \beta$, reheating will lead to diffusion controlled $\alpha \rightarrow \beta$ transformation with a kinetics described by the JMA equation generalised to anisothermal processes (Equation 22). If, on the other hand, the microstructure is martensitic, heating up the material into the tempering range (> 400 °C) will cause the decomposition of $\alpha^{'}$ into a mixture of α and β. This transformation is also diffusion controlled and its kinetics are also described by the JMA equation (Equation 18). The values of k and n in Equation 18 for this reaction were determined by Mur et al. (Mur et al., 1996). If the decomposition is incomplete, tempering results in a three-phase microstructure consisting of $\alpha^{'} + \alpha + \beta$.

3.3 Phase transformations during second cooling

During cooling down to room temperature at cooling rates lower than 410 °C/s β phase decomposes into α by a diffusion controlled mechanism. For cooling rates in excess of 410 °C/s β may undergo a martensitic transformation or be retained at room temperature, depending on the volume fraction of this phase in the alloy. Several authors have observed that β is completely retained upon quenching if its proportion in the alloy is lower than 0.25, because the β phase is enriched in vanadium, a β stabiliser (Fan, 1993; Lee et al., 1991; R. Castro, 1966). If the volume fraction is higher than 0.25 a proportion of β given by (Fan, 1993):

$$f_r = 0.25 - 0.25.f_\beta(T_0), \tag{25}$$

is retained at room temperature, where $f_b(T_0)$ is the volume fraction of β prior to quenching. The remaining β ($f_b(T_0) - f_r$) undergoes a martensitic transformation. As a result, cooling an alloy consisting only of β phase at rates higher than 410 °C/s originates a fully martensitic structure, while materials with smaller volume fractions of this phase retain a variable proportion of β (Figure 3). Thus, the martensite volume fraction is given by:

$$f_{\alpha'}(T) = f_{\alpha'}(T_0) + (f_\beta(T_0) - f_r)\left[1 - exp\left(-\gamma(M_s - T)\right)\right], \tag{26}$$

with $f_{\alpha'}(T_0)$ the volume fraction of $\alpha^{'}$ phase present in the alloy prior to quenching. Similar phase transformations will occur during subsequent thermal cycles and the final microstructure will result from all the consecutive transformations occurring at each point.

3.4 Calculation of mechanical properties

The Young's modulus and hardness were calculated from the phase constitution of the alloy using the rule of mixtures (Costa et al., 2005; Fan, 1993; Lee et al., 1991). The Young's moduli of α, β and $\alpha^{'}$ are 117, 82 and 114 GPa respectively and the Vickers hardnesses are 320, 140 and 350 HV.

4. Results

4.1 Experimental confirmation

The model was first validated by comparing the calculation results with the experimental distributions of microstructure and properties found in Ti-6Al-4V walls produced by laser powder deposition (LPD), a rapid manufacturing technique that uses a focused laser beam to melt a stream of metallic powder and deposit the molten material continuously at precise locations (Laeng et al., 2000; R.Vilar, 1999; 2001).

4.1.1 Simulation results

The model was applied to simulate the phase transformations occurring during the deposition of a 75 layer Ti-6Al-4V wall with 0.32 mm width, 10.00 mm length and 3.50 mm height, represented in Figure 5. The scanning speed was 4 mm/s, the laser beam diameter 0.3 mm, the idle time between the deposition of consecutive layers 6 s and the initial substrate temperature 20 °C. The laser beam power was varied according to the plot of Figure 6.a, reflecting the power adjustments performed by a closed loop online control system utilised during the manufacture of the experimental sample, which acts to keep the size of the melt pool generated by the laser beam at the surface of the workpiece constant. An initial beam power of 130 W was used and progressively decreased with each new deposited layer up to the 20th layer, where a beam power of 50 W was reached and kept constant for the rest of the process. An average absorptivity of 15 % was considered in the calculations, according to the results of Hu *et al.* (Hu & Baker, 1999) regarding the laser deposition of Ti-6Al-4V using a CO_2 laser.

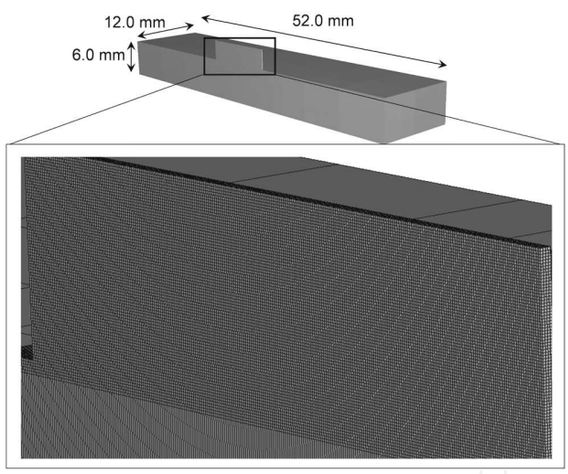

Fig. 5. View of the substrate and the wall with a detail of the wall mesh.

The calculated phase distribution is shown in Figures 6.b and 7. The highest volume fractions of α and β phases (0.03 and 0.07 respectively) occur close to the substrate, and decrease as the distance from the substrate increases, reaching zero in the uppermost layers of the part. Conversely, the volume fraction of martensite is lowest near the substrate (approximately 0.9) and has a maximum at the top of the wall, where the structure is fully martensitic. The cooling rates experienced by the material during the deposition process are always higher than 410 °C/s (Figure 8.a), and, as a consequence, after solidification the material undergoes a martensitic transformation during cooling to room temperature. Figure 8.a

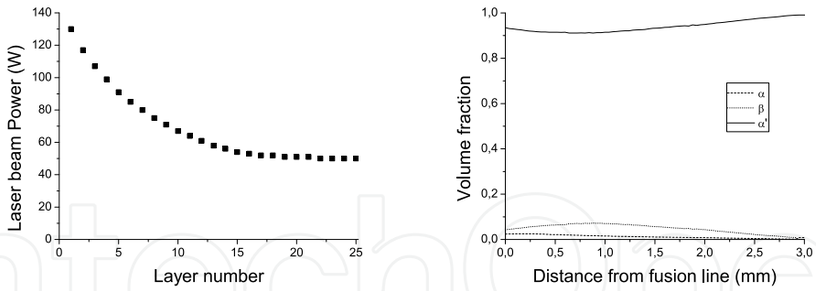

(a) (b)

Fig. 6. (a) Laser beam power used to deposit each layer. (b) Phase constitution as a function of the distance from the fusion line.

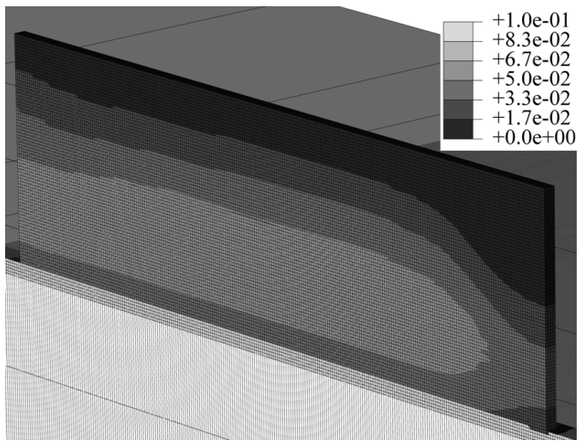

Fig. 7. β phase distribution.

shows that the cooling rate progressively decreases as the number of layers increases and asymptotically approaches a value below the martensite critical cooling rate (410 °C/s). Therefore, the deposition of additional layers would likely lead to the suppression of the martensitic transformation in the top layers of the part.

The thermal cycles originated by layer overlap heat up the previously deposited material to temperatures in the tempering range ($T > 400$°C), causing the progressive decomposition of the martensite into α and β (Figure 8.b).

The idle time between the deposition of consecutive layers used (6 s) is too short to allow the part to cool down to room temperature before the deposition of a new layer. As a result the temperature of the workpiece increases progressively as the deposition advances, eventually stabilising at approximately 270 °C after the deposition of the 15th layer, as depicted in the plot of Figure 9.a.

This facilitates tempering because, as heat accumulates in the part, the material residence time in the tempering temperatures range increases from less than 1 s in the first cycles to approximately 4 s from the 15th cycle onwards (Figure 9.b).

The cumulative effect of the consecutive thermal cycles is sufficient for significant tempering to take place, particularly in the layers deposited at the beginning of the buildup process. For example, the material in the first layer is subjected to 74 thermal cycles subsequent to

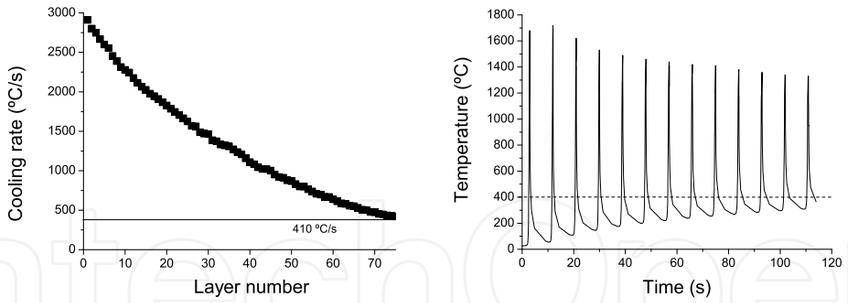

(a) (b)

Fig. 8. (a) Cooling rates experienced by the material deposited in the different layers. (b) Temperature evolution of the material deposited in the first layer for the first 120 s of the fabrication process. Tempering of the martensite takes place at temperatures higher than 400 °C.

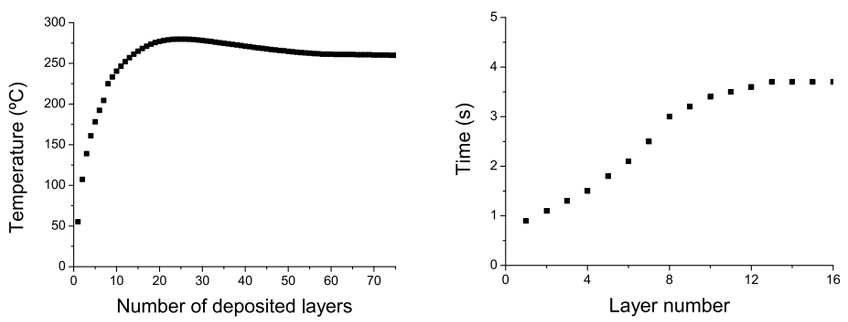

(a) (b)

Fig. 9. (a) Temperature evolution of the interface between the wall and the substrate after the deposition of each layer. (b) Time above 400 °C during the deposition of each layer, measured at the interface between the wall and the substrate.

its deposition, which amounts to approximately 250 s in the tempering range, leading to a decomposition of approximately 10% of the previously formed martensite. The evolution of the phase constitution of the material is presented in Figure 9.a and the Young's modulus and hardness variations along the wall height are presented in Figure 10.b

4.1.2 Experimental results

The distributions of microstructure, Young's modulus and hardness predicted by the model were compared to the values measured on a sample manufactured with similar processing parameters to validate the model. The system used in the experimental tests was developed by C. Meacock and R. Vilar (Meacock, 2009) to manufacture small to medium size parts for biomedical applications and the experimental work described in this section was carried out in collaboration with these authors. The system uses a CO_2 laser with a maximum beam power of 130 W which can be focused to a spot of 0.3 mm in diameter by means of a ZnSe lens with a focal length of 63.5 mm. The system employs a closed loop online control system whereby

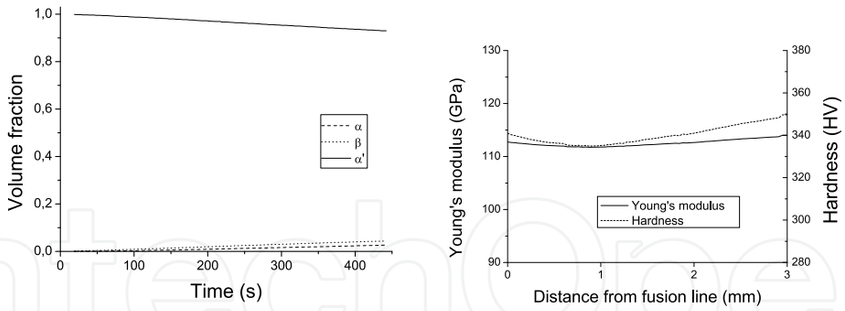

(a) (b)

Fig. 10. (a) Evolution of the phase constitution of the material in the first layer. (b) Distribution of properties along the wall height.

the intensity of the infra-red radiation emitted in the range 1.0-1.7 μm is monitored by a GaAs In doped photodiode. The acquired information is processed by a control function which acts to adjust the laser power in order to maintain constant melt pool dimensions during buildup, allowing for a high stability and dimensional accuracy in the manufacture of the parts. The deposition was conducted using a Ti-6Al-4V powder with a particle size in the range 25-75 μm fed through a capillary at a mass flow rate of 0.14 g/min.

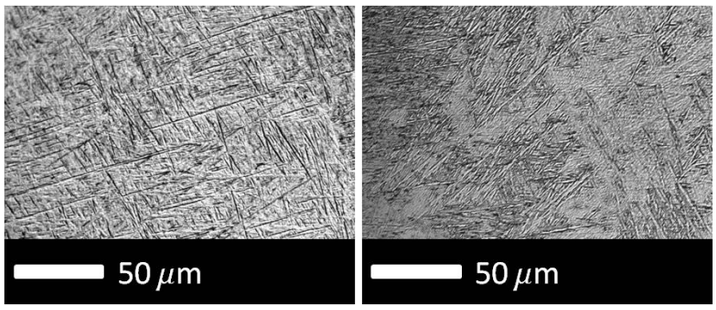

(a) (b)

Fig. 11. (a) Optical micrograph taken approximately 250 μm from the wall apex. (b) Optical micrograph taken approximately 500 μm from the fusion line. Adapted from C. Meacock (Meacock, 2009)

An optical micrograph of the cross section of the manufactured sample reveals an acicular morphology in the upper region of the wall (Figure 11.a). This is observed in the last 15 layers and is consistent with the hexagonal α'-martensite microstructure of Ti-6Al-4V, which typically presents a morphology consisting of long orthogonally oriented plates. Close to the bottom of the wall, the material presents a different microstructure (Figure 11.b), consisting of martensite needles interspersed with regions of $\alpha + \beta$. To quantify the volume fraction of the different phases, X-ray diffraction was conducted on the deposited material. The volume fraction of β phase was calculated from the X-ray diffractograms by the direct comparison method, with the error being the standard deviation of the averaged intensities method (Meacock, 2009). The volume fraction of β phase decreases with increasing distance to the substrate from 0.06 at 0.5 mm to 0.04 at 2.5 mm (Figure 12.a). The β phase results primarily

from the tempering of martensite, which is a slow process when compared to the typical time scales involved in laser processes. However, the deposition of the 75 layers takes approximately 450 s, which is long enough for tempering to occur and a noticeable volume fraction of β phase is observed in the deposited material.

The Young's modulus and hardness of the material were measured by depth sensing indentation testing carried out on the longitudinal section of the wall at 1 mm intervals starting at a distance of 0.5 mm from the fusion line, and the results are presented in Figures 12.b and 12.c, respectively. The Young's modulus is seen to increase slightly with increasing distance from the fusion line, from 110 GPa at 0.5 mm to 114 GPa at 2.5 mm. Likewise, the hardness increases with increasing distance from the fusion line, from 330 HV at a distance of 0.5 mm to 365 HV at 2.5 mm. The values of β volume fraction, Young's modulus and hardness calculated by the model are compared to the experimental values and plotted as a function of the distance from the fusion line in Figure 12.

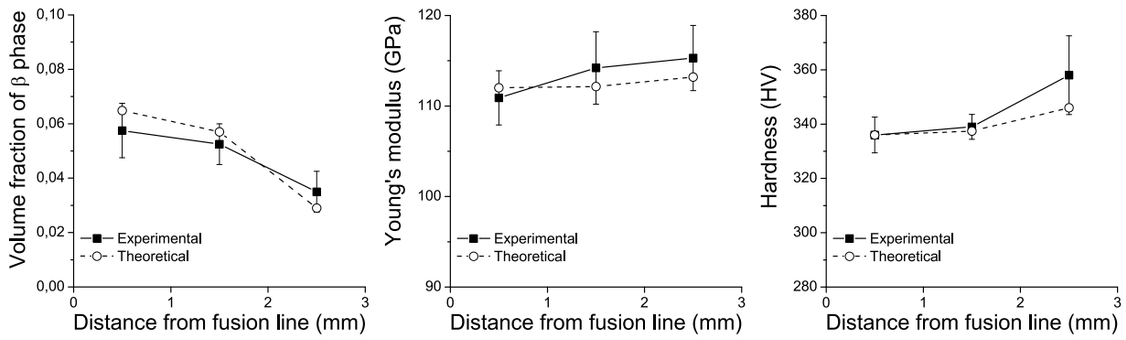

Fig. 12. Comparison between the values obtained using the model and the experimental measurements for: (a) volume fraction of β phase, (b) Young's modulus and (c) Vicker's hardness.

The variation of the volume fraction of β along the height of the wall is small but compares well with the values predicted by the model. The calculated Young's modulus and hardness show an overall good correlation with the experimental values and are within the experimental error limits, although the Young's modulus varies only slightly in the material.

5. Development of processing maps

To optimise the deposition process in order to obtain parts fulfilling specific requirements it is necessary to assess how the choice of processing parameters affects the properties of the deposited material. To this end, the model was used to obtain processing maps relating the scanning speed (v), idle time between the deposition of consecutive layers (Δt) and substrate temperature (T_{sub}) to the microstructure, hardness and Young's modulus distributions in parts produced by laser powder deposition. A summary of these results has been published elsewhere (Crespo & Vilar, 2010) but a more detailed analysis of the heat transfer and metallurgical phenomena is presented in this section. A thin wall geometry was considered with a width of 1 mm, a length of 14 mm and a height of 5 mm, produced by overlapping 10 layers of Ti-6Al-4V on a substrate of the same material with the dimensions 100*25*140 mm (Figure 13). The deposition was assumed to take place along the longitudinal

direction of the substrate and on its mid plane so that a symmetry plane exists and only half of the geometry needs to be considered for calculation purposes. A laser beam with a power P = 1000 W focused to a spot d_{beam} = 1.5 mm in diameter (at e^{-2} of the maximum intensity) was used so that a melt pool of approximately 1 mm in diameter is created in the laser / material interaction zone, matching the track width. An average absorptivity of 15 % was used in the calculations, assuming the utilisation of a CO_2 laser (Hu & Baker, 1999).

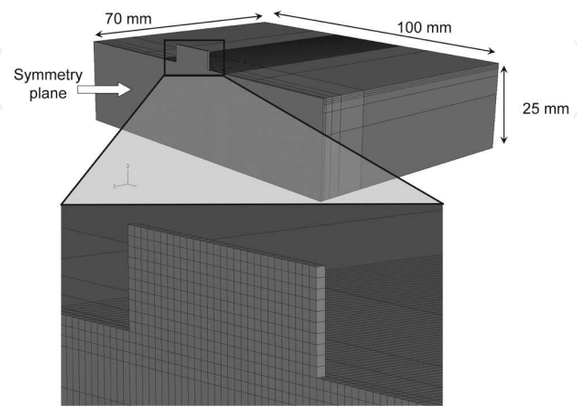

Fig. 13. Finite element mesh.

5.1 Influence of scanning speed and idle time

Figure 14 shows the computed Young's modulus and hardness distributions along the wall height using a scanning speed of 20 mm/s and an idle time of 10 s. The final part presents a fully martensitic microstructure and uniform distributions of Young's modulus and hardness, 114 GPa and 350 HV, respectively (Figure 14). During the fabrication process the material undergoes cooling rates in excess of 10^3 °C/s, which favour the transformation of the β phase formed upon solidification by a martensitic mechanism. Some tempering occurs due to re-heating caused by the overlapping of the following layers, but its extent is small because it takes several minutes for significant martensite decomposition to occur, whereas the residence time of the material within the tempering temperature range (above 400 °C) during the complete build-up process is less than 10 s (around 1 s for each subsequently deposited layer, Figure 15). A 10 s idle time is sufficient for the part to cool down to approximately 20 °C before the deposition of each new layer, therefore the average substrate temperature increases only slightly during build-up of the part (Figure 15). Using lower idle times leads to a progressive increase of the workpiece temperature during the deposition process (Figure 16.a), but the deposited material still presents a martensitic microstructure because the cooling rates are not significantly affected by the temperature increase in the part at the scanning speed used (20 mm/s). For this scanning speed the cooling rates are much higher than the critical cooling rate for the martensitic transformation (410 °C/s) and asymptotically approach a limit value between 1500 °C/s (for Δt = 2 s) and 1900 °C/s (for $\Delta t > 30$ s) as the number of deposited layers increases (Figure 16.b).

Another critical parameter to play a role in the formation of the microstructure of the material is the scanning speed used to perform the manufacture. Low values of this parameter can cause the suppression of the martensitic transformation because they lead to longer interaction times between the heat source (laser radiation) and the material, allowing more time for heat

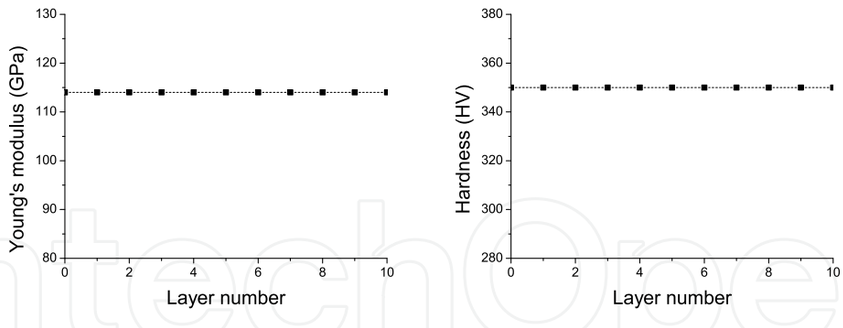

Fig. 14. (a) Young's modulus (GPA) and (b) Vickers hardness (HV) distributions in a part produced using a scanning speed of 20 mm/s.

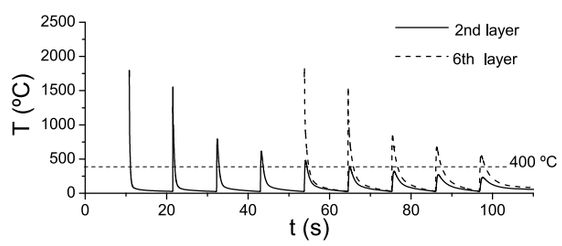

Fig. 15. Temperature variation during build-up for the 2nd and 6th layers of deposited material. The total time above 400 °C, where tempering takes place, is approximately 1s for each of the 5 layers deposited subsequently, which is not sufficient for significant tempering to occur.

to be conducted away from the interaction zone and reducing the temperature gradient in the wall, as shown in Figure 17. As a consequence of heat conduction to the substrate being the main mechanism of heat extraction from the interaction zone, a lower temperature gradient in the build direction slows down the heat flow, causing a reduction of the cooling rate which is approximately given by:

$$\frac{\partial T}{\partial t} = \frac{k}{c_p \rho} \frac{\partial^2 T}{\partial x^2}, \tag{27}$$

where xx' is the build-up (vertical) direction. Figure 18.a shows the variation of the cooling rate experienced during the deposition of the 10^{th} layer of material, with the scanning speed for two different values of the idle time. For low scanning speeds, the material in the last layers cools from above the β-transus at rates lower than 410 °C/s and the martensitic transformation is replaced by the diffusional $\beta \rightarrow \alpha$ transformation, leading to a microstructure composed of 0.92 α + 0.08 β in this region (Figure 18.b). As a result, the final part presents a non-uniform distribution of hardness, 350 HV in the bottom layers and 305 HV

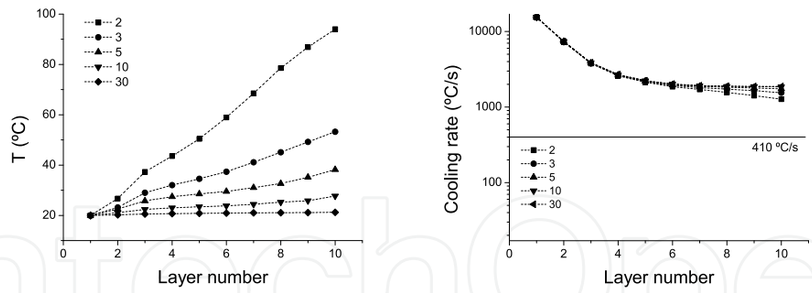

Fig. 16. (a) Average temperature in the part immediately before the deposition of each layer for different values of idle time, v_{scan} = 20 mm/s and an initial substrate temperature of 20 °, and (b) cooling rates experienced by the material in each of the layers deposited (plotted in logarithmic scale).

in the upper region (Figure 19.b). The Young's modulus is practically uniformly distributed (Figure 19.a), 113 GPa in the lower region (practically only α') and 114 GPa in the upper layers (0.92 α + 0.08 β), because α and α' have similar Young's modulus and the proportion of β in the alloy is very low. From the plot of Figure 18.a it is apparent that scanning speeds equal to 12 mm/s or higher result in cooling rates above 410 °C/s and lead to β transforming by a martensitic mechanism, originating an α' structure. Scanning speeds lower than 12 mm/s lead to lower cooling rates and to parts with two microstructurally distinct regions, a bottom region composed of α', and a top region composed of 0.92 α and 0.08 β, resulting from the diffusion controlled $\beta \rightarrow \alpha$ transformation.

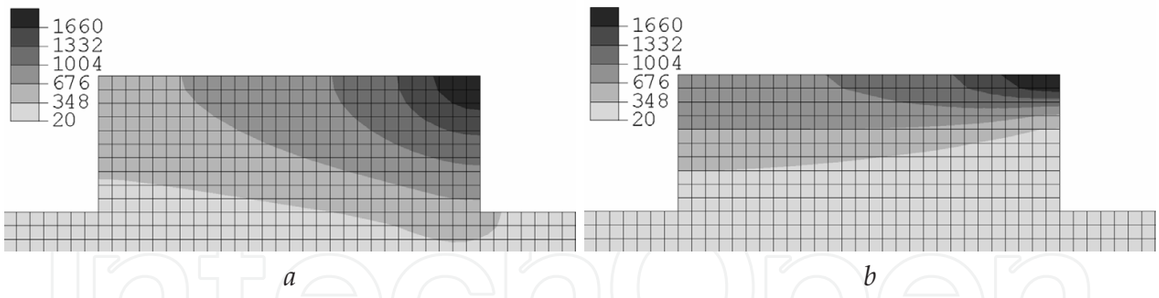

Fig. 17. Temperature (°C) distribution at the end of the last deposition step using scanning speeds of (a) 5mm/s and (b) 20 mm/s. 20 mm/s. Adapted from Crespo and Vilar (Crespo & Vilar, 2010)

5.2 Influence of substrate temperature

In addition to the scanning speed and idle time, the substrate temperature has an important influence on the microstructure and properties of the material. Increasing the temperature of the substrate has two principal effects:

1. Firstly, pre-heating the substrate to temperatures close to or above M_f (400 °C) gives rise to different microstructures because the material cannot complete the martensitic

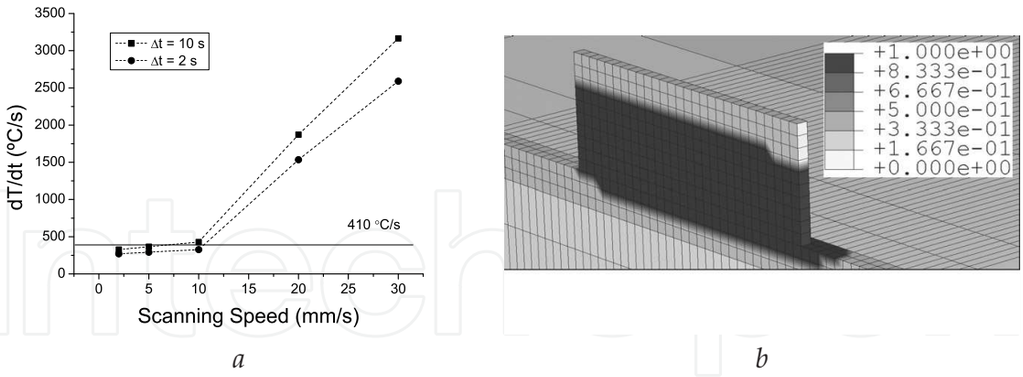

a *b*

Fig. 18. (a) Cooling rate experienced by the material deposited in the last layer as a function of the scanning speed for Δt = 2 s and Δt = 10 s; (b) volume fraction of martensite in the microstructure of a part fabricated using a scanning speed of 5 mm/s.

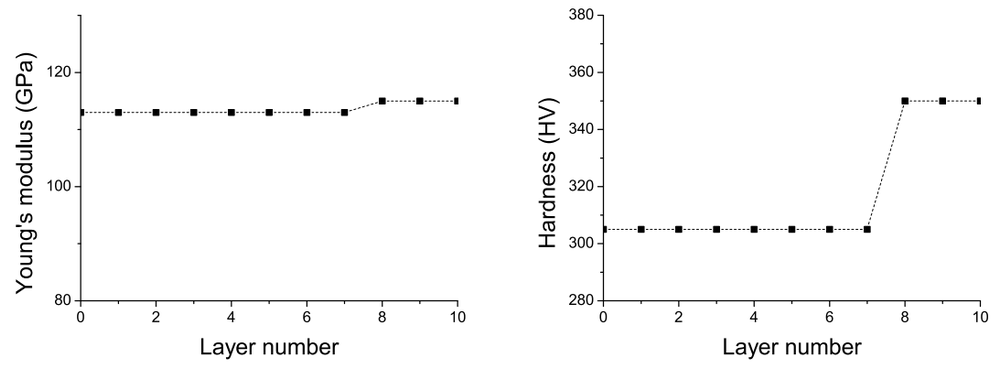

a *b*

Fig. 19. (a) Young's modulus (GPA) and (b) Vickers hardness (HV) distributions in a part fabricated using a scanning speed of 5 mm/s.

transformation before the deposition of the next layer. For example, if the substrate is pre-heated to 500 °C, the $\beta \rightarrow \alpha'$ transformation is stopped at about 75% of its extent, and at this temperature vanadium diffuses into the β phase (less than 20 s are necessary to achieve a concentration of 10 wt.%), stabilising and retaining this phase upon cooling to room temperature and leading to a material with roughly 0.75 of α and 0.25 of β (Fan, 1993; Katzarov et al., 2002; Malinov, Markovsky, Sha & Guo, 2001);

2. Secondly, increasing the temperature of the substrate acts to reduce the temperature gradient throughout the material. This leads to lower cooling rates which facilitate the decomposition of β into α by a diffusional process.

The joint influence of the scanning speed, idle time and substrate temperature on the final microstructure and properties of the parts is best analysed in terms of processing maps that relate this information. One of the most relevant applications of the model is the construction

of such processing maps to allow the prediction of the microstructure of the material and its properties given any set of processing parameters. The maps in Figure 20.a and 20.b (Crespo & Vilar, 2010) show the dependence of the cooling rate on the scanning speed and on the idle time for substrate temperatures of 20 and 500 °C, respectively, and allow finding the processing windows leading to specific microstructures.

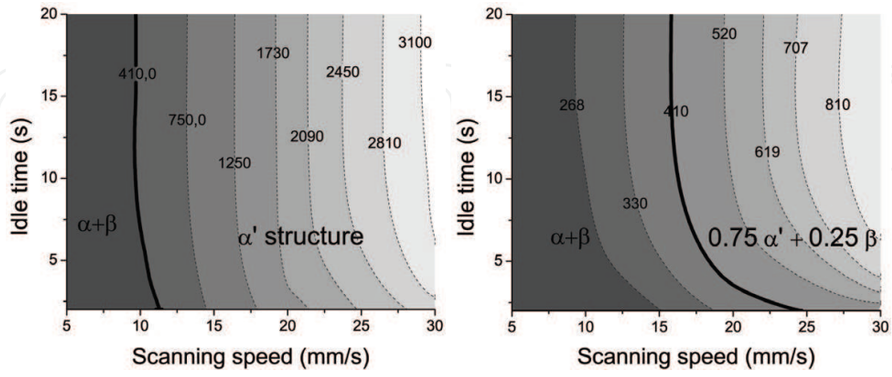

Fig. 20. (a) Contour plot of the cooling rate as a function of v and Δt for $T_{sub} = 20°C$. The cooling rate is mostly dependent on the scanning speed, as evidenced by the constant cooling rate lines being almost vertical. (b) Contour plot showing the dependence of the cooling rate on the scanning speed and the idle time using a substrate pre-heated to 500 $°C$. Adapted from Crespo and Vilar (Crespo & Vilar, 2010).

For example, when the deposition takes place on a substrate pre-heated at 500 °C, a scanning speed of 20 mm/s results in a martensitic transformation if an idle time of 5 s is used, while for 16 mm/s, idle times longer than 15 s are necessary to achieve the martensite critical cooling rate. More generally, any set of parameters to the right of the bold line ($\partial T/\partial t = 410°C/s$) shown in the plot of Figure 20.b leads to a martensitic transformation in the material. For these sets of parameters, after the deposition of the last layer, the material is at 500 °C and its microstructure consists approximately of 0.75 α' + 0.25 β, with a vestigial proportion of α formed during tempering. During cooling to room temperature, the β phase remains stable and is retained due to the enrichment in vanadium and the final part has a uniform microstructure containing 0.75 α' + 0.25 β (Fan, 1993). This material presents a uniform hardness of 300 HV and a Young's modulus of 106 GPa, which is the minimum that can be obtained for the Ti-6Al-4V alloy. The distributions of Young's modulus and Vickers hardness are shown in Figure 21.a and b, respectively.

These results are in agreement with results published by other authors. In particular the diffusional transformation of β phase in Ti-6Al-4V components produced by laser assisted deposition at low scanning speeds was verified by Kelly et al. (v=0.625 - 2.5 mm/s) (Kelly & Kampe, 2004a) and Qian et al. (v=6.7 - 10.0 mm/s) (Qian et al., 2005), whereas the occurrence of a martensitic transformation at higher speeds was confirmed by Groh (d. Groh, 2006).

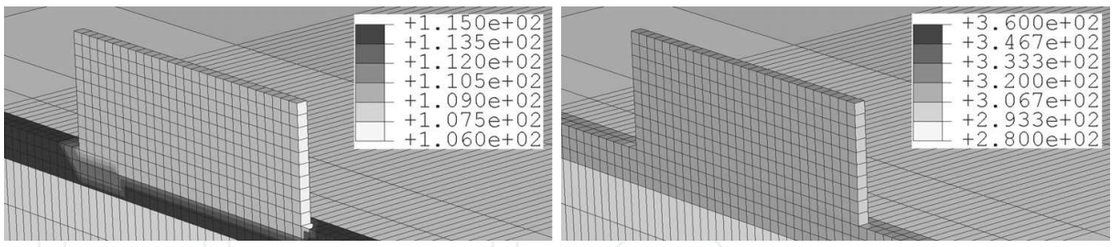

Fig. 21. (a) Young's modulus (GPA) and (b) Vickers hardness (HV) distributions in a part fabricated using a scanning speed of 15 mm/s on a substrate at 500 °C. Adapted from Crespo and Vilar (Crespo & Vilar, 2010).

6. Conclusion

A thermo-kinetic finite element model coupling heat transfer calculations and phase transformation kinetics theory which predicts the microstructure and properties distributions in titanium parts produced by rapid manufacturing was developed. The results of the model were compared to experimental measurements of the phase constitution and properties performed on samples produced by a laser based technique using identical parameters to the ones utilised in the model and showed a good agreement. The model was also applied to the development of processing maps relating the deposition parameters to the microstructure and properties of the parts. From the results achieved it was concluded that:

1. Computational methods are an efficient way to study heat transfer and the associated metallurgical phenomena which occur during manufacture of components;
2. This type of approach provides a cheap and rapid way to construct processing maps for the optimisation of fabrication processes;
3. Pre-heating the substrate allows controlling the final distribution of microstructure and properties in Ti-6Al-4V parts produced by rapid manufacturing;
4. By changing the processing parameters during the build-up process it possible to control the properties in Ti-6Al-4V produced by rapid manufacturing processes

6.1 Future work

The model can be easily modified to describe the microstructural transformations of other Ti alloys. In the case of α/β alloys these modifications simply amount to changing the kinetic parameters used to describe the various transformations simulated in the model and future work will include the application of the model to simulate the microstructural evolution of different titanium alloys. The phase transformations kinetics subroutine is a generic algorithm that describes the phase transformations of Ti-6Al-4V as a function of the heat treatment and is not specific to rapid manufacturing processes. This subroutine can be used to describe other processing techniques and, more generally, any heat treatment of the Ti-6Al-4V alloy. Additionally, more experimental work will be carried out to achieve a thorough validation of the model for different processing conditions.

7. Acknowledgements

The author thankfully acknowledges the valuable help and contributions from Dr. C. Meacock and Prof. R. Vilar.

8. References

Bontha, S., Klingbeil, N. W., Kobryn, P. A. & Fraser, H. L. (2006). Thermal process maps for predicting solidification microstructure in laser fabrication of thin-wall structures, *Journal of Materials Processing Technology* 178: 135–142.

Boyer, R., Welsch, G. & Coolings, E. W. (1994). *Materials Properties Handbook : titanium alloys*, ASM International.

Brunette, D. M. (2001). *Titanium in Medicine*, Springer.

Costa, L., Vilar, R., Reti, T. & Deus, A. M. (2005). Rapid tooling by laser powder deposition: Process using finite element analysis, *Acta Materialia* 14: 3987–3999.

Crespo, A. (2010). *Mathematical Simulation of Laser Powder Deposition Applied to the Production of Prosthesis and Implants of Ti and Ti-6Al-4V*, PhD thesis, Instituto Superior Técnico.

Crespo, A., Deus, A. M. & Vilar, R. (2006). Finite element analysis of laser powder deposition of titanium, *Proceedings of ICALEO 2006-25th International Congress on Applications of Lasers and Electro-Optics*, Scottsdale, Arizona, pp. 1016–1021.

Crespo, A., Deus, A. M. & Vilar, R. (2008). Modeling of phase transformations and internal stresses in laser powder deposition, *Proceedings of GCL-HPL 2008*, Lisbon, Portugal, pp. 713120–713120–10.

Crespo, A. & Vilar, R. (2010). Finite element analysis of the rapid manufacturing of ti-6al-4v parts by laser powder deposition, *Scripta Materialia* 63: 140–143.

d. Groh, H. C. (2006). Development of laser fabricated Ti-6Al-4V, *Technical report*, National Aeronautics and Space Administration John H. Glenn Research Center.

Desai, C. S. & Abel, J. F. (1972). *Introduction to the Finite Element Method*, Van Nostrand Reinhold Company.

Deus, A. M. & Mazumder, J. (2006). Three-dimensional finite element models for the calculation of temperature and residual stress fields in laser cladding, *Proceedings of ICALEO 2006-25th International Congress on Applications of Lasers and Electro-Optics*, Scottsdale, Arizona, pp. 496–505.

Donachie, M. J. (2004). *Titanium, A Technical Guide - 2nd Edition*, ASM International.

Elmer, J. W., Palmer, T. A., Babu, S. S., Zhang, W. & DebRoy, T. (2004). Phase transformations dynamics during welding of Ti-6Al-4V, *Journal of Applied Physics* 95: 8327–8339.

Fan, Z. Y. (1993). On the young moduli of Ti-6Al-4V alloys, *Scripta Metallurgica Et Materialia* 29: 1427–1432.

Ghosh, S. & Choi, J. (2005). Three-dimensional transient finite element analysis for residual stresses in the laser aided direct metal/material deposition process, *Journal of Laser Applications* 17: 144–158.

Hu, C. & Baker, T. N. (1999). A semi-empirical model to predict the melt depth developed in overlapping laser tracks on a Ti-6Al-4V alloy, *Journal of Materials Processing Technology* 94: 116–122.

Kahlen, F. J. & Kar, A. (2001). Residual stresses in laser-deposited metal parts, *Journal of Laser Applications* 13: 60–69.

Katzarov, I., Malinov, S. & Sha, W. (2002). Finite element modeling of the morphology of beta to alpha phase transformation in Ti-6Al-4V alloy, *Metallurgical and Materials Transactions A* 33: 1027–1040.

Kelly, S. & Kampe, S. (2004a). Microstructural evolution in laser-deposited multilayer Ti-6Al-4V builds: Part I. microstructural characterization, *Metallurgical and Materials Transactions A* 35: 1861–1867.

Kelly, S. & Kampe, S. (2004b). Microstructural evolution in laser-deposited multilayer Ti-6Al-4V builds: Part II. thermal modeling, *Metallurgical and Materials Transactions A* 35: 1869–1879.

Koistinen, D. P. & Marburger, R. E. (1959). A general equation prescribing the extent of the austenite-martensite transformation in pure iron-carbon alloys and plain carbon steels, *Acta Metallurgica* 7: 59–60.

Labudovich, M., Hu, D. & Kovacevic, R. (2003). A three dimensional model for direct laser metal powder deposition and rapid prototyping, *Journal of Materials Science* 38: 35–49.

Laeng, J., Stewart, J. G. & Liou, F. W. (2000). Laser metal forming processes for rapid prototyping - a review, *International Journal of Production Research* 38(16): 3973–3996.

Lee, Y. T., Peters, M. & Welsch, G. (1991). Elastic-moduli and tensile and physical-properties of heat-treated and quenched powder metallurgical Ti-6Al-4V-alloy, *Metallurgical and Materials Transactions A* 22: 709–714.

Leyens, C. & Peters, M. (2003). *Titanium and Titanium Alloys*, Wiley-VCH.

Malinov, S., Guo, Z., Sha, W. & Wilson, A. (2001). Differential scanning calorimetry study and computer modeling of beta double right arrow alpha phase transformation in a Ti-6Al-4V alloy, *Metallurgical and Materials Transactions A* 32: 879–887.

Malinov, S., Markovsky, P., Sha, W. & Guo, Z. (2001). Resistivity study and computer modelling of the isothermal transformation kinetics of Ti-6Al-4V and Ti-6Al-2Sn-4Zr-2Mo-0.08Si alloys, *Journal of Alloys and Compounds* 314: 181–192.

Meacock, C. (2009). *Laser Powder Microdeposition of Biomedical Alloys*, PhD thesis, Instituto Superior Tecnico.

Mur, F. X. G., Rodriguez, D. & Planell, J. A. (1996). Influence of tempering temperature and time on the alpha'-Ti-6Al-4V martensite, *Journal of Alloys and Compounds* 234: 287–289.

Neto, O. O. D. & Vilar, R. (2002). Physical-computational model to describe the interaction between a laser beam and a powder jet in laser surface processing, *Journal of Laser Applications* 14: 46–51.

Polmear, I. J. (1989). *Light Alloys*, Edward Arnold.

Qian, L., Mei, J., Liang, J. & Wu, X. (2005). Influence of position and laser power on thermal history and microstructure of direct laser fabricated Ti-6Al-4V samples, *Materials Science and Technology* 21: 597–605.

R. Castro, L. S. (1966). Contribution to metallographic and structural study of titanium alloy ta6v, *Memoires Scientifiques de la Revue De Metallurgie* 63: 1025–1058.

Reddy, J. N. (2006). *An Introduction to the Finite element Method*, McGraw-Hill.

Reddy, J. N. & Gartling, D. K. (1994). *The Finite Element Method in Heat Transfer and Fuid Dynamics*, CRC Press.

R.Vilar (1999). Laser cladding, *Journal of Laser Applications* 11(2): 64–79.

R.Vilar (2001). Laser cladding, *International Journal of Powder Metallurgy* 37(2): 31–48.

S. Denis, D. Farias, A. S. (1992). Mathematical-model coupling phase-transformations and temperature evolutions in steels, *Isij International* 32: 316–325.

Toyserkani, E., Khajepour, A. & Corbin, S. (2004). 3-d finite element modeling of laser cladding by powder injection: effects of laser pulse shaping on the process, *Optics and Lasers in Engineering* 41: 849–867.

Vasinonta, A., Beuth, J. L. & Grifith, M. (2001). A process map for consistent build conditions in the solid freeform fabrication of thin-walled structures, *Journal of Manufacturing Science and Engineering - Transactions of the AIME* 123(4): 615–622.

Wang, L., Felicelli, S., Gooroochurn, Y., Wang, P. & Horstemeyer, M. (2008). Optimization of the lens process for steady molten pool size, *Materials Science and Engineering A* 474: 148–156.

Yoshiki, O. (2007). *Bioscience and Bioengineering of Titanium Materials*, Elsevier.

Zienkiewicz, O. C. & Taylor, R. L. (2000). *The Finite Element Method*, Butterwoth Heinemann.

Convection and Conduction Heat Transfer

Edited by Dr. Amimul Ahsan

ISBN 978-953-307-582-2
Hard cover, 394 pages
Publisher InTech
Published online 17, October, 2011
Published in print edition October, 2011

The convection and conduction heat transfer, thermal conductivity, and phase transformations are significant issues in a design of wide range of industrial processes and devices. This book includes 18 advanced and revised contributions, and it covers mainly (1) heat convection, (2) heat conduction, and (3) heat transfer analysis. The first section introduces mixed convection studies on inclined channels, double diffusive coupling, and on lid driven trapezoidal cavity, forced natural convection through a roof, convection on non-isothermal jet oscillations, unsteady pulsed flow, and hydromagnetic flow with thermal radiation. The second section covers heat conduction in capillary porous bodies and in structures made of functionally graded materials, integral transforms for heat conduction problems, non-linear radiative-conductive heat transfer, thermal conductivity of gas diffusion layers and multi-component natural systems, thermal behavior of the ink, primer and paint, heating in biothermal systems, and RBF finite difference approach in heat conduction. The third section includes heat transfer analysis of reinforced concrete beam, modeling of heat transfer and phase transformations, boundary conditions-surface heat flux and temperature, simulation of phase change materials, and finite element methods of factorial design. The advanced idea and information described here will be fruitful for the readers to find a sustainable solution in an industrialized society.

InTech Europe
University Campus STeP Ri
Slavka Krautzeka 83/A
51000 Rijeka, Croatia
Phone: +385 (51) 770 447
Fax: +385 (51) 686 166

InTech China
Unit 405, Office Block, Hotel Equatorial Shanghai
No.65, Yan An Road (West), Shanghai, 200040, China
中国上海市延安西路65号上海国际贵都大饭店办公楼405单元
Phone: +86-21-62489820
Fax: +86-21-62489821

IntechOpen

IntechOpen